

Integrated Photonic Devices and Materials Group

Academic and Research Staff

Professor Leslie A. Kolodziejski, Dr. Gale S. Petrich, Principal Research Scientist

Graduate Students

Solomon Assefa, Reginald E. Bryant, Alexei A. Erchak, Yamini Kangude, Aleksandra Markina, Sarah J. Rodriguez, Sheila N. Tandon, and Ryan D. Williams

Technical and Support Staff

Diane W. Hagopian and Rachel Cohen

Introduction

The emphasis of the research program is the design, epitaxial growth, device fabrication and characterization of a number of photonic and opto-electronic structures. The epitaxial growth of the heterostructures is performed in the laboratory consisting of two gaseous source epitaxy reactors interconnected to several smaller chambers, which are used for sample introduction and in-situ surface analysis.

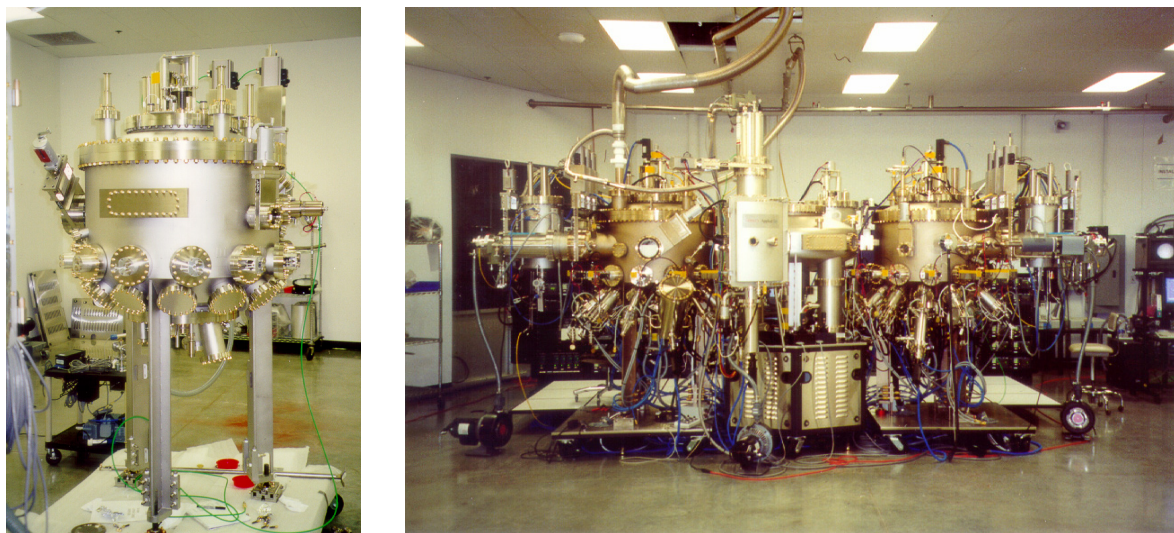


Figure 1. The left image shows the growth reactor prior to its integration onto the system. The right image shows the system during system acceptance at the factory.

The laboratory has recently purchased and taken the title of a new Veeco GEN 200 solid source, dual-reactor molecular beam epitaxy system (Figure 1). The new system will allow for the epitaxial growth of dilute nitrides and antimony-based films in addition to arsenide- and phosphide-based films. The system platens can hold multiple 3" or 4" wafers, or a single 6" or 8" wafer. The system incorporates a low wobble manipulator that will allow in-situ feedback control of the epitaxial processes using optical sensors such as band edge absorption and spectroscopic ellipsometry. The system is currently awaiting the completion of the new laboratory at MIT to house the epitaxy tool.

In the following sections, the status of the various III-V-based projects will be discussed. The existing Riber III-V gas source molecular beam epitaxy system is utilized for the development of GaAs-based bipolar cascade lasers, for the fabrication of GaAs-based devices implementing one- and two-dimensional photonic bandgap crystals within their structure and for the development of electromechanical optical switches. The development of bipolar cascade lasers represents a collaboration between the research groups under the direction of Prof. Rajeev Ram and Prof. Leslie Kolodziejski. The research projects utilizing photonic crystals in addition to the development of the optical switch represents

the combined efforts of the research groups led by Professors John D. Joannopoulos (Theory), Leslie A. Kolodziejski (Fabrication), Henry I. Smith (Fabrication), and Erich P. Ippen (Measurement). The complexity of the design, fabrication and characterization of these photonic crystal-based structures necessitates a strong interaction between the various research groups.

1. Development of Bipolar Cascade Laser with an Emission Wavelength of 0.98 μm

Sponsors

DARPA/Brown University: #1123-24596

Project Staff

Ryan D. Williams, Aleksandra Markina, Dr. Gale S. Petrich, Professor Rajeev Ram and Professor Leslie A. Kolodziejski

The bipolar cascade laser design aims to combine two or more lasing active regions in epitaxial series. Previous work realized operable cascade lasers at 980 nm. Currently, the work has focused on transitioning the design from using quantum wells that emit at 980 nm to quantum dots that emit at 1300 nm, as well as improving the characteristics of the reverse-biased tunnel junction, which connects the consecutive active regions.

As 1300 nm is an important wavelength in telecommunications, recent work has focused on obtaining InAs quantum dots on GaAs substrates. InAs quantum dots extend the range of achievable emission wavelengths of GaAs-based active devices well into the functional telecommunications regime. Furthermore, quantum dots allow for the realization of ultra-low laser threshold currents, narrow emission spectra, improved gain properties, and increased temperature stability. Photoluminescence studies have shown strong emission between 1250-1300 nm (Figure 2). Careful control of the growth conditions such as substrate temperature and deposition rate have allowed precise control over the emission wavelength and intensity. Atomic force microscopy has been used to confirm the presence of quantum dots and has shown their average diameter to be around 20 nm as shown in Figure 3.

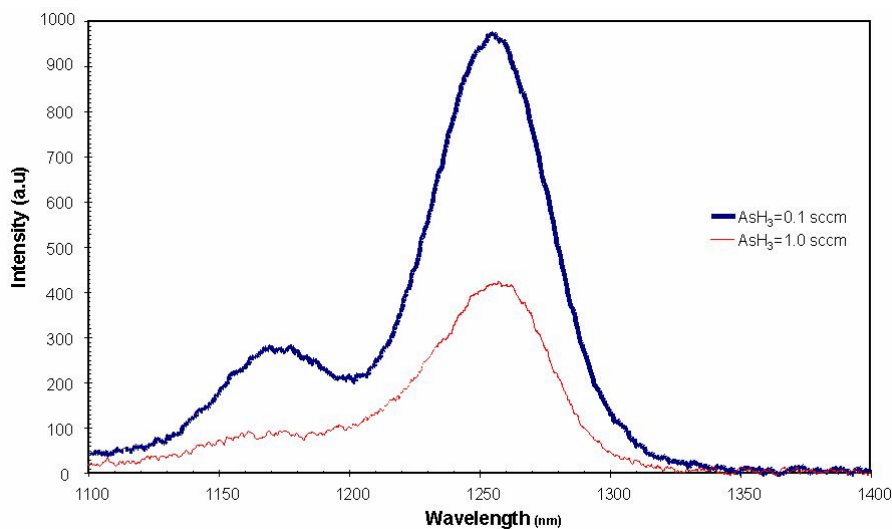


Figure 2. Photoluminescence from quantum dots versus arsine flow rates: 1.0 sccm (thin line) and 0.1 sccm (thick line).

The introduction of indium into the GaAs tunnel junction material is theorized to improve the differential resistance of the junction and thereby increase the tunneling current, resulting in improved quantum efficiency for the laser. Samples have been grown by gas source molecular beam epitaxy and processed to examine the effects of indium-incorporation and are currently undergoing electrical testing. Prior Hall effect measurements have confirmed the presence of extremely high doping levels in the tunnel junction

materials, a requirement for tunneling operation. Bipolar cascade lasers using 980 nm emitting quantum wells have been integrated with indium-containing tunnel junctions and are undergoing processing for later testing.

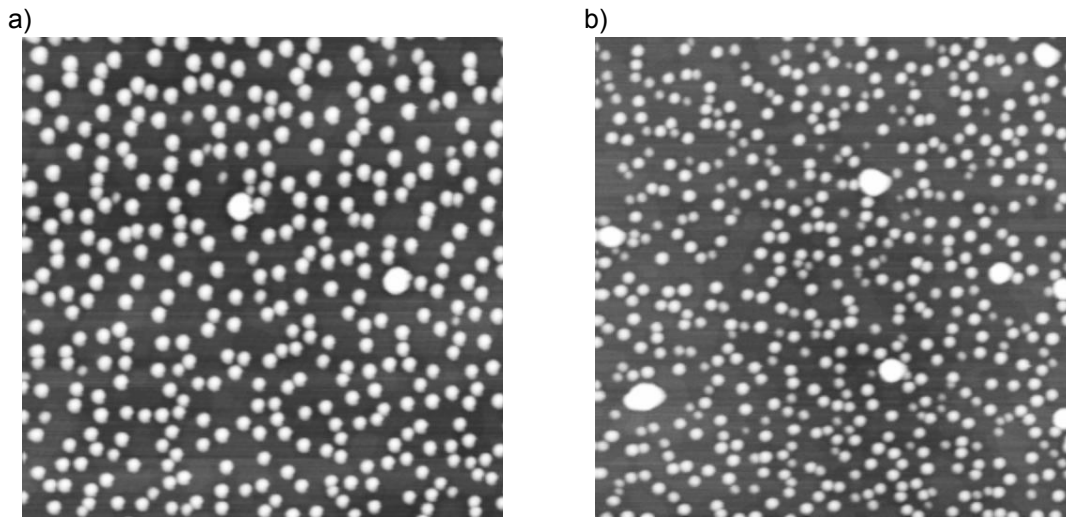


Figure 3. Atomic force micrographs of 1 μm x 1 μm square areas. a) With the arsine flow =0.1 sccm, the density of InAs quantum dots is $4.2 \times 10^{10} \text{ cm}^{-2}$ and the average diameter is 23 nm. b) With the arsine flow =1.0 sccm, the density of InAs quantum dots is $6.2 \times 10^{10} \text{ cm}^{-2}$ and the average diameter is 21 nm.

The current aim of the project is to produce a bipolar cascade laser on a GaAs substrate containing quantum dot active regions and operating at 1300 nm shown schematically in Figure 4. Laser structures have been grown and are currently undergoing processing and testing.

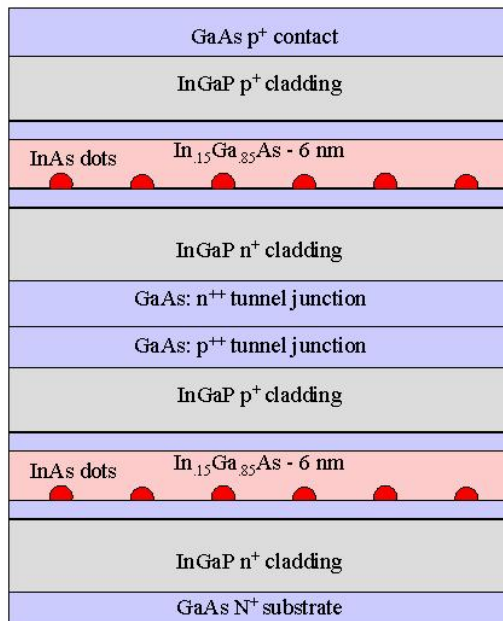


Figure 4. Schematic of a bipolar cascade laser with quantum dot active regions.

2. Towards Optical Logic

Sponsors

Lincoln Laboratory: #BX-8372
 Lincoln Laboratory: #BX-8506

Project Staff

Aleksandra Markina, Sarah J. Rodriguez, Dr. Gale S. Petrich and Professor Leslie A. Kolodziejski,

Currently, network services impose bottlenecks on optical fiber communications. While network management complexity increases with the number of wavelengths that the fibers carry, most signal processing operations, such as switching and routing, are still performed electronically after opto-electronic (OE) conversion [1]. An average internet packet transverses 16 nodes, with OE-EO conversions for electronic switching at each node. The development of ultrafast all-optical logic would make it possible to avoid multiple conversions and to distribute low-level network functionality in the optical core. High-level slow electronic processing would then be pushed to network edges. Desired functionality of all-optical signal processing includes routing, synchronization, header processing, and cascability. Developing a family of optical logic with complete Boolean functionality (an optical equivalent of Transistor-Transistor Logic) will be an important step in this direction.

This project includes the design of epitaxially-grown heterostructures that will form the basis for the optical circuit, the optimization of passive components as well as the semiconductor optical amplifiers (SOA), a discussion regarding the issue of integrating active and passive components together on a single platform and the design and analysis of an optical logic "unit cell". The proposed optical logic unit cell is based on an integrated balanced Mach-Zehnder interferometer with a SOA in each arm. The unit cell will be designed for ultrafast 2x2 crossbar operation with an ideal extinction ratio and will be capable of performing a complete set of Boolean operations (AND, INV and XOR). Although the basic implementation does not address the issues of timing, reflections, and wavelengths contention, resolving these issues is crucial in order to ensure the cascability of individual unit logic cells.

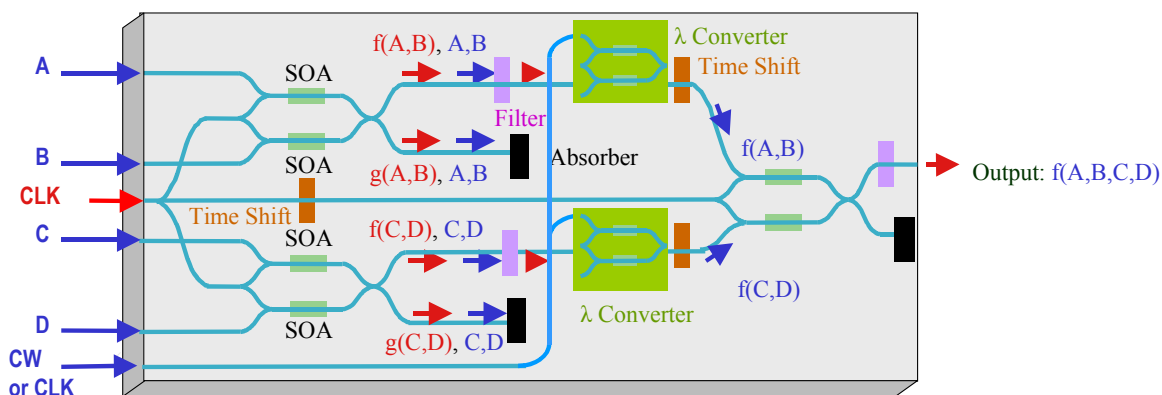


Figure 5. Three unit cells cascaded on a chip with additional devices that enable proper signal processing.

A schematic illustration of cascading multiple Mach-Zehnder interferometer-based "unit cells" together to perform $(A \text{ xor } B) \text{ xor } (C \text{ xor } D)$ is presented in Figure 5. The circuit consists of three "unit cells": $(A \text{ xor } B)$, $(C \text{ xor } D)$ and the last stage. However, in order to operate properly, this optical circuit requires a number of additional devices. Time delays are used in order to equalize the optical path lengths in order to control the timing, while filters remove unwanted wavelengths, such as those used for the clock signal or control signals. Additionally, wavelength converters can be employed to resolve ambiguity between the data and the control signals. Absorbers can be inserted to eliminate the back reflections into the logic stages. Multiple wavelength clocks/control signals are required for cascading optical logic elements.

3. Coupling into Photonic Crystal Waveguides

Sponsors

National Science Foundation #DMR-0213682

Project Staff

Solomon Assefa, Alexei A. Erchak, Peter Rakich, Dr. Steven G. Johnson, Mark Mondol, Dr. Peter Bienstman, Dr. Gale S. Petrich, Professor Erich P. Ippen, Professor John D. Joannopoulos, Professor Henry I. Smith and Professor Leslie A. Kolodziejski

Large-scale photonic integrated circuits require guiding light around sharp bends with a radius of curvature on the order of a wavelength. In conventional index-guided waveguides, light is confined as a result of total internal reflection at the interface between the high refractive index waveguiding layer and its low index surroundings. However, using these conventional index contrast waveguides in integrated circuits would be difficult because they are susceptible to large optical losses as the bend's radius of curvature decreases. Photonic crystals (PCs), which consists of a periodic arrangement of high and low-dielectric constant material, have been proposed as a potential solution in order to guide light around corners including 90° bends with near perfect transmission.

One such two-dimensional (2D) photonic crystal consists of an array of cylindrical rods of high dielectric material above a low dielectric material. Introducing a line defect, such as a row of smaller radius cylinders, into the 2D photonic crystal results in a linear waveguide. The 2D periodic arrangement of dielectric rods surrounding the line defect contains a photonic band gap (PBG), i.e. a range of frequencies in which light can not propagate. Thus, an optical signal with a frequency inside the PBG has its energy confined within the line defect and is evanescent within the photonic crystal. The radius of the cylinders in the line defect remains large enough to provide index guiding in the third dimension (normal to the plane of periodicity). The localization of a mode inside the line defect can be utilized to guide light around sharp corners including a 90° bend with low optical loss as illustrated in Figure 3.

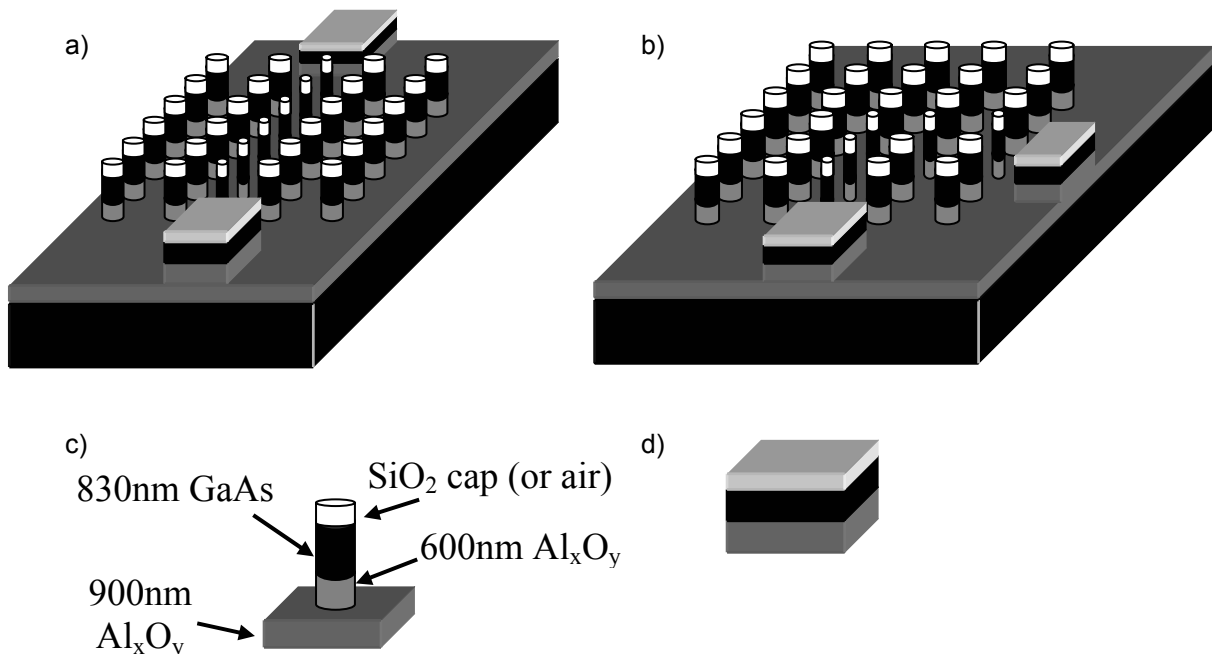


Figure 6. (a) Schematic of a linear PC waveguide. (b) Schematic of a 90° bend PC waveguide. (c) Schematic of a cylindrical pillar structure. For the bulk photonic crystal, the diameter of the pillar is 300nm; for the defects, the diameter is 250nm. (d) Input/output waveguide.

Nevertheless, the practical use of photonic crystal waveguides is limited due to the poor coupling efficiency between the photonic crystal waveguide, and the conventional index-guided waveguide. Coupling poses a challenge because the photonic crystal waveguide exhibits a significantly different mode profile and propagation mechanism compared to traditional waveguides that use index confinement. In the conventional waveguide, the field has only forward propagating components, while the field in the photonic crystal waveguide has both forward and backward propagating components due to scattering. Furthermore, guiding in the conventional waveguide is in the high index core that is surrounded by a low index material; in the photonic crystal waveguide, guiding is in a low index core that is surrounded by two photonic crystal mirrors.

Figure 7 compares three different designs for coupling into the defect photonic crystal waveguide. The design in Figure 7(a) suffers from Fabry-Perot reflection at the edges of the photonic crystal region, which makes the transmission of the waveguide dependent on the photonic crystal waveguide length. By tapering the end of input and output index waveguides as shown in Figure 7(b), the reflections can be reduced. In the third design [Figure 7(c)], the input waveguide is adiabatically converted into a strongly coupled cavity waveguide. This adiabatically transforms the forward propagating component of the field into both forward and backward propagating components before reaching the photonic crystal. Also, the cladding is introduced slowly from the edge, thereby adiabatically transforming the mode from high-index guiding to gap guiding. 2D simulations show that this coupling scheme results in almost 100% transmission through the photonic crystal waveguide.

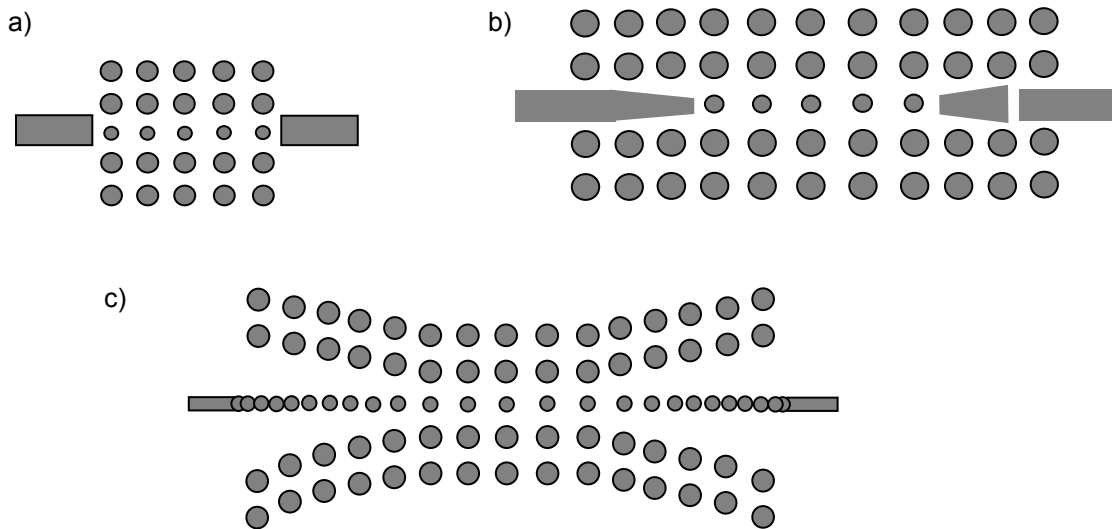


Figure 7. (a) Schematic of coupling from untapered dielectric waveguides. (b) Schematic of coupling from a tapered dielectric waveguides. (c) Schematic of adiabatic transition from a dielectric waveguide into strongly coupled cavities and tapered cladding.

The cylindrical rods of the photonic crystal consist of a high-index, 830nm epitaxial GaAs layer sandwiched between a 100nm thick SiO₂ cap layer and a 600nm thick low-index Al_xO_y layer. An additional 900nm thick Al_xO_y layer is below the cylindrical rods isolating the GaAs guiding layer from the GaAs substrate. The heterostructure is grown using gas source molecular beam epitaxy on a (100) GaAs substrate. The Al_xO_y is initially grown epitaxially as Al_{0.9}Ga_{0.1}As.

The fabrication process commences by sputtering a 400nm thick SiO₂ layer on the sample. Next, the waveguide and photonic crystal are defined using direct-write electron-beam lithography. Each sample is coated with polymethylmethacrylate (PMMA) electron beam resist, and each cylinder is defined by

exposing a square pattern. The finite width of the beam rounds-off the corners of each square yielding a circular hole upon development. Simulations show that the largest band gap is obtained from a periodic arrangement of rods with diameter of 300nm. Exposure-dose experiments are done to determine the optimal parameters for the exposures. As shown in Figure 8, a dose of $536 \mu\text{C}/\text{cm}^2$, current of 250pA, and clock frequency of 0.20 MHz gave hole diameters close to the desired values. The input and output coupling waveguides and different sized arrays of holes are written by stitching together $250\mu\text{m} \times 250\mu\text{m}$ fields.

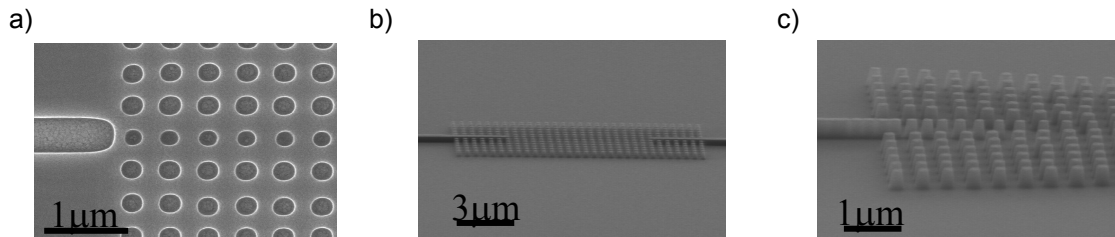


Figure 8. (a) Top view scanning electron microscope (SEM) image of the coupling design from Figure 7(a) after e-beam lithography in PMMA. The bulk photonic crystal has hole diameter of 307nm, while the defect has diameter of 244nm. (b) Top view SEM image of the coupling design from Figure 7(b) after SiO_2 etch. (c) Top view SEM image of the coupling design from Figure 7(c) after SiO_2 etch.

A 50 nm thick nickel film is evaporated on the sample after the PMMA is developed, and a liftoff process is performed. The pattern is transferred to the SiO_2 by reactive-ion etching (RIE) in a CHF_3 plasma after which the nickel mask is removed using a nickel etchant. Using the SiO_2 mask, the cylindrical rods are created by etching the GaAs and the AlGaAs to a total depth of $1.5 \mu\text{m}$ in a BCl_3/He plasma. Experiments were done using various metal masks as an alternative to the SiO_2 mask. However, the metal masks sputtered or degraded during the long duration of the GaAs/AlGaAs etch. Next, each sample is lapped and cleaved in order to create a smooth input facet to promote the efficient coupling of a test signal with a wavelength of $1.55\mu\text{m}$. Finally, the AlGaAs is transformed into Al_xO_y using a wet thermal oxidation process. Figure 9 shows a side view of the bulk photonic crystal.

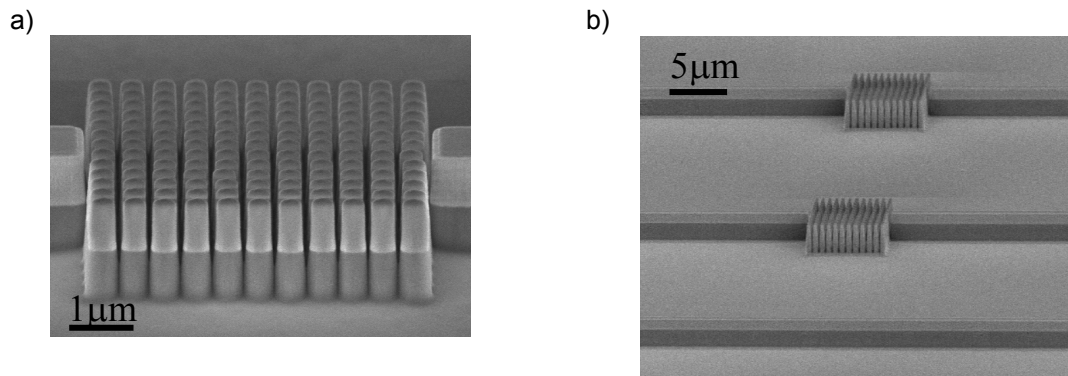


Figure 9. (a) Side view SEM image of a bulk photonic crystal etched in GaAs/AlGaAs using BCl_3/He plasma. The AlGaAs is oxidized into Al_xO_y . The period is 500nm and the diameter of the pillars is 300nm. The input and output waveguides are $1.5\mu\text{m}$ wide. (b) Photonic crystal devices on a single chip. The design contains a straight waveguide for normalization purposes.

Currently, the photonic crystal devices are being tested. The band gap is being mapped first by varying the number of columns in a bulk photonic crystal. Also, the three coupling mechanisms are being compared to confirm the best transmission through the photonic crystal waveguide.

4. Design and Fabrication of a Superprism Using Two-Dimensional Photonic Crystals

Project Staff

Sheila N. Tandon, Chiyan Luo, Dr. Marin Soljacic, Michael E. Walsh, Dr. Gale S. Petrich, Professor John D. Joannopoulos, Professor Henry I. Smith and Professor Leslie A. Kolodziejski

Sponsor

DARPA/Rockwell Science Center: #B1F431652

A superprism is an optical device similar to a conventional prism only with two enhanced properties: (1) super-dispersion and (2) ultra-refraction. Just as a conventional prism separates light into multiple wavelengths, a superprism separates these wavelengths over wider angles--termed "super-dispersion." A superprism can also be used to magnify the angle of propagation of a single wavelength of light to steer the beam over a wide range of angles--termed "ultra-refraction." Photonic crystals form the essence of the superprism effect. Being able to realize these superprism effects would be very useful for a number of applications ranging from enhanced devices for wavelength division multiplexed (WDM) systems to a new class of ultra-refractive optical elements for beam manipulation.

The device consists of a two-dimensional photonic crystal with a square lattice of cylindrical air holes in a high index material such as silicon or gallium arsenide. The top view schematic of the device shape is shown in Figure 10. The device is hexagonal-shaped with the photonic crystal (PC) occupying a square region in the center. The input and output facets of the device are shown. The initial design has focused on realizing ultra-refraction such that an input angular sweep of approximately +/- 2 degrees is amplified to about +/- 30 degrees at the output for a wavelength of 3.2 μm. A thick low index layer is used to minimize radiation loss into the high index substrate.

The feature sizes of the photonic crystal can be scaled depending on the wavelength of operation as shown in Figure 10. The desired wavelengths of 3.1μm and 1.55μm imply hole lattice constants of 750nm and 372nm, and hole radii of 300nm and 150nm, respectively. The total thickness of the device (excluding the substrate) is about 3.5 microns (460nm GaAs, 3mm Al_xO_y) while the top surface will have an area of about 2 x 2cm.

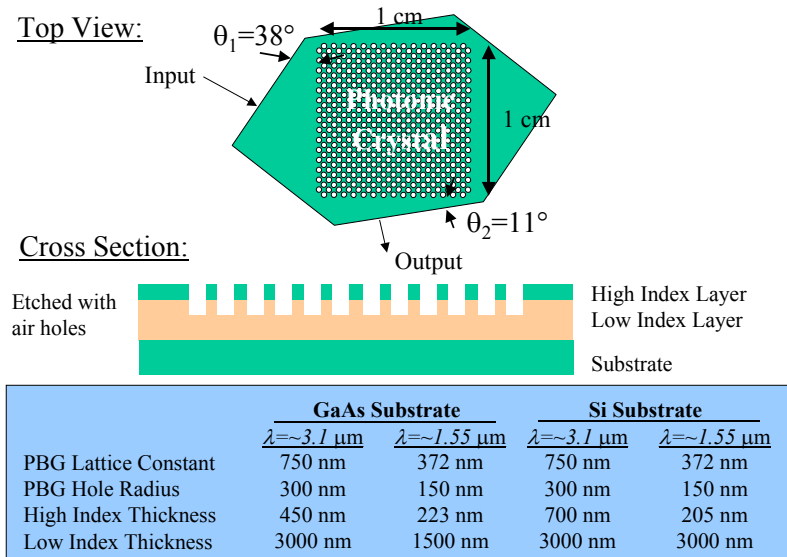


Figure 10. Superprism device design showing top and side views of the device.

The hexagonal device shape is patterned using photolithography while the photonic crystal holes are patterned using interference lithography. After each lithography step, patterns are etched into the hard mask layers via reactive ion etching (RIE). The fully patterned hard mask layers are then used to etch the substrate material via another RIE step. Figure 11(a) shows a digital photograph of the patterned hard mask layers on a silicon substrate. Two hard mask layers have been used: 50nm chromium on top of 250nm HSQ (spin-on oxide). The chromium layer is patterned with the superprism hexagonal shape while the open square area is patterned with the $\sim 780\text{nm}$ period photonic crystal in HSQ. The diffraction pattern from the PC can be seen as the streak across the square area.

Figure 11(b) shows a microscope image (100x magnification) of the corner region of the photonic crystal area. The unit cell of the PC is rotated 45 degrees with respect to the square region. The alignment accuracy between the photonic crystal orientation and the square region is critical for superprism performance. Figure 11(b) shows how a line of PC holes is aligned to the square edge with an accuracy of less than one degree thus achieving the necessary tolerance.

Future work includes calibrating the photonic crystal hole size during the interference lithography exposure, determining a more robust hard mask layer other than chromium due to post-wet etch residue, and reactive ion etching of the silicon substrate material via reactive ion etching.

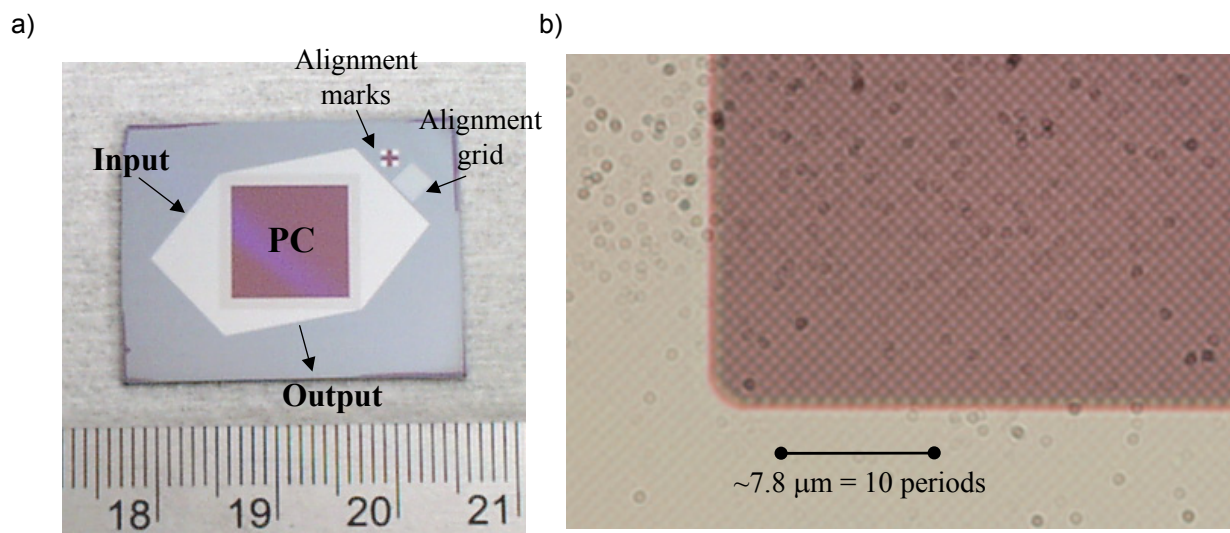


Figure 11. (a) Digital photograph showing a top view of the superprism hard mask layers on a silicon substrate. (b) Microscope image of the corner area of photonic crystal region. Please note that the microscope lens has dust particles that can not be removed.

5. Oxidation of AIAs Layers for Large Area Broadband Saturable Bragg Reflectors

Sponsors

Office of Naval Research #N00014-021-0717

Project Staff

Sheila N. Tandon, Alexei A. Erchack, Juliet T. Gopinath, Thomas R. Schibli, Dr. Gale S. Petrich, Prof. Leslie A. Kolodziejski, Prof. Franz X. Kaertner, and Prof. Erich P. Ippen

Semiconductor saturable Bragg-reflectors (SBRs) are important components for the generation of femtosecond pulses from ultra fast laser systems [2]. In order to create shorter pulses, it is necessary to use mirrors with a wider bandwidth. An alternative to GaAs/AIAs mirrors, is to monolithically integrate absorbers onto broadband GaAs/ Al_xO_y Bragg-mirrors, created by the steam oxidation of GaAs/AIAs.

AlAs is converted to Al_xO_y using a wet oxidation system that is schematically shown in Figure 12. Steam flows over the sample, which is located in a quartz tube furnace at an elevated temperature between 400°C and 450°C . A constant flow of N_2 through a flask of deionized water maintained at a constant temperature of 90°C introduces the water vapor into the furnace. Syphens are used to prevent the water levels in the flask and surrounding bath from falling over the duration of the oxidation allowing for oxidation times of up to 12 hours.

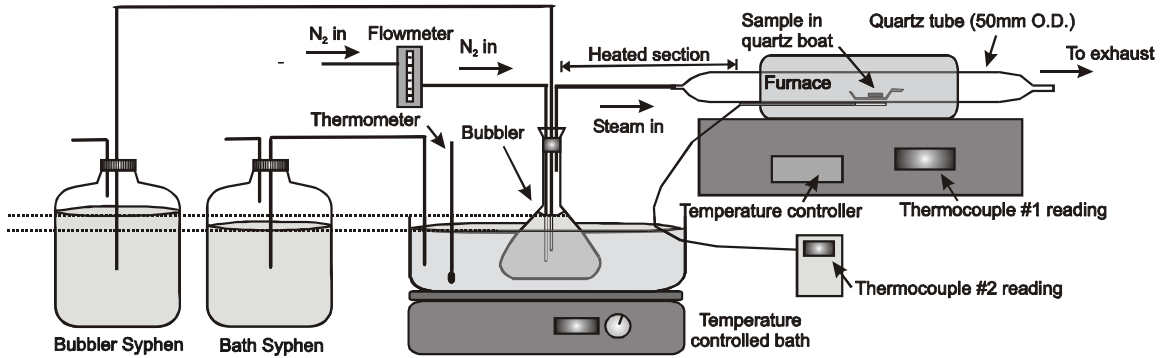


Figure 12. Schematic of the wet oxidation setup.

Figure 13(a) and (b) show top and side views of a $500\mu\text{m}$ diameter SBR with a GaAs/ Al_xO_y mirror stack created through the oxidation of GaAs/AlAs layers [3]. The top view shows a fully-oxidized $500\mu\text{m}$ diameter SBR. However, oxidation at 435°C for 3.5 hours resulted in delamination between the layers as shown in the side view. This delamination is possibly due to a number of factors; one of which is the weak bonding between GaAs and Al_xO_y .

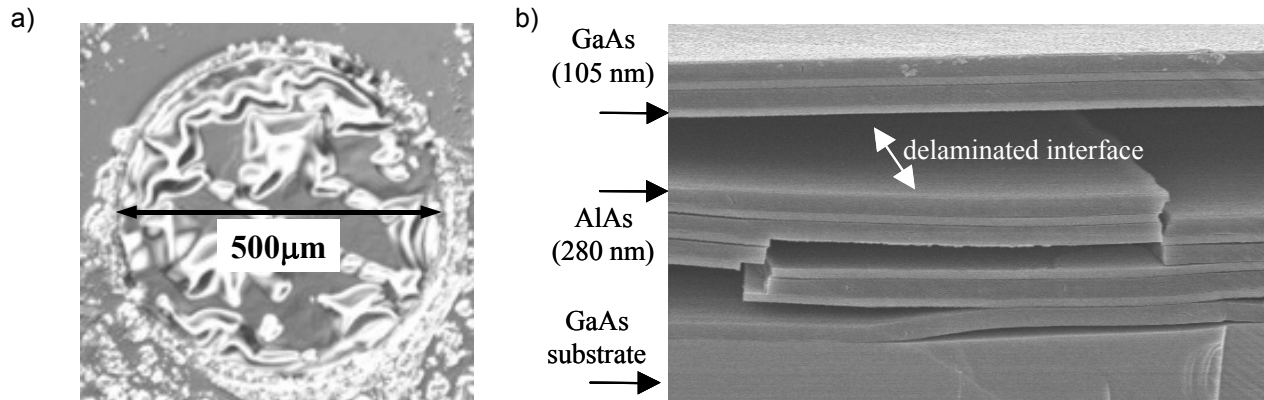


Figure 13. (a) Top view SEM image of mesa structure oxidized at 435°C for 3.5 hours. (b) Cross-sectional SEM image showing the GaAs/AlAs layers with delaminated interfaces.

By using low Al content AlGaAs layers instead of GaAs, the bonding between layers can be strengthened resulting in a stable mirror stack after oxidation. Figure 14(a) and (b) show top and side views of an SBR design that uses $Al_{0.3}Ga_{0.7}As/AlAs$ layers [4]. The top view shows a fully-oxidized $500\mu\text{m}$ diameter SBR that has not experienced delamination. The cross-section shows the absorber layers consisting of an InGaAs quantum well between two GaAs buffer layers, and a 7 pair mirror stack of $Al_xO_y/Al_{0.3}Ga_{0.7}As$. For oxidation temperatures between 415°C and 435°C , the mirror stack was successfully oxidized without delamination. At higher temperatures, oxidation of the structure was limited by delamination of the absorber layer at the SBR edges possibly due to interfacial strain. At 420°C the mirror was completely

oxidized in 4 hours without absorber delamination. Using $\text{Al}_{0.3}\text{Ga}_{0.7}\text{As}$ as the mirror's high index layer strengthens bonding between layers upon oxidation, while preventing significant oxidation of this layer.

In conclusion, saturable absorbers can be integrated with broadband Bragg-mirrors using epitaxial growth and the steam oxidation of AIAs layers. By using low Al content AlGaAs layers as the high index material in the dielectric stack, interfacial bonding is strengthened permitting the stable oxidation of large areas

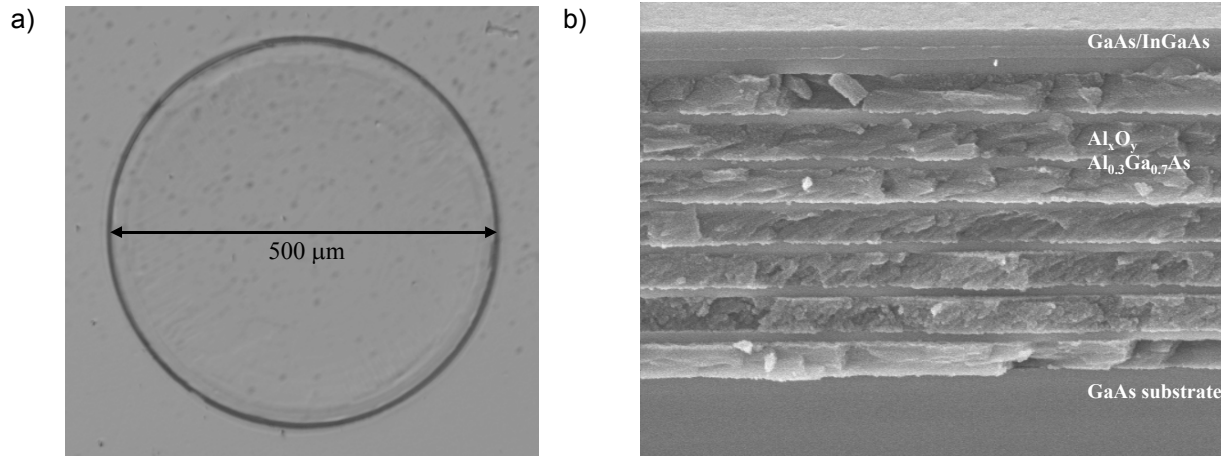


Figure 14. (a) Nomarski image of fully-oxidized SBR. (b) SEM image of SBR cross-section showing 67 nm GaAs, 40nm InGaAs, 67 nm GaAs absorber with a 7 pair $\text{Al}_x\text{O}_y/\text{Al}_{0.3}\text{Ga}_{0.7}\text{As}$ mirror stack (~180nm/92nm).

6. Optical Nano-Mechanics

Sponsors:

National Science Foundation #DMR-9808941

Project Staff

Reginald E. Bryant, Solomon Assefa, Peter Rakich, Michelle L. Povinelli, Dr. Steven G. Johnson, Dr. Gale S. Petrich, Professor Erich P. Ippen, Professor John D. Joannopoulos, and Professor Leslie A. Kolodziejski

A major focus of optical engineering research is to bring optical systems to the large-scale functionality of electrical systems. Striving to reach this objective, a variety of optical devices are currently being developed in an aluminum gallium arsenide III-V material system. The III-V material system is the choice optical bench in which these optical devices are being developed due to advances in material engineering, which allows nanometer precision of high index contrasting layers, ranging from oxidized aluminum arsenide to gallium arsenide. As a result of such precision, a variety of optical manipulations can be carried out with nanometer-sized devices at micron-sized wavelengths. Presently, the focus has been set upon the deployment of nanometer-sized electromechanical-actuated waveguide devices with the prospect of broadening the functionality of integrated optical systems. These devices are termed optical nanoelectromechanical devices (ONEM devices).

The ONEM device that is currently being developed, routes optical energy between two adjacent waveguides by lateral coupling after an electrostatic mechanical deflection of the waveguides from an applied voltage, as schematically shown in Figure 15. Initially, in a ground state (zero applied voltage), a distance of g_0 separates the waveguides. The initial g_0 separation is defined using electron beam lithography. The initial distance of g_0 is set as to not allow for any lateral coupling between the two adjacent waveguides. A potential difference is then applied to both waveguides, which then reduces the separation of the waveguides.

The initial separation of g_0 and the deflected separation of g_{couple} are determined from optical simulations and electromechanical simulations of the two-waveguide system. The g_0 separation and g_{couple} separation are contingent upon the width, thickness, length, and geometry of the two waveguides. Due to the dynamic relation arising from the optics and the electromechanics of the ONEM device, iterations of both types of simulations are being done for a variety of configurations in order to optimize design trade-offs between the optical and electromechanical operations. Figure 16 shows some prototypes of the ONEM device.

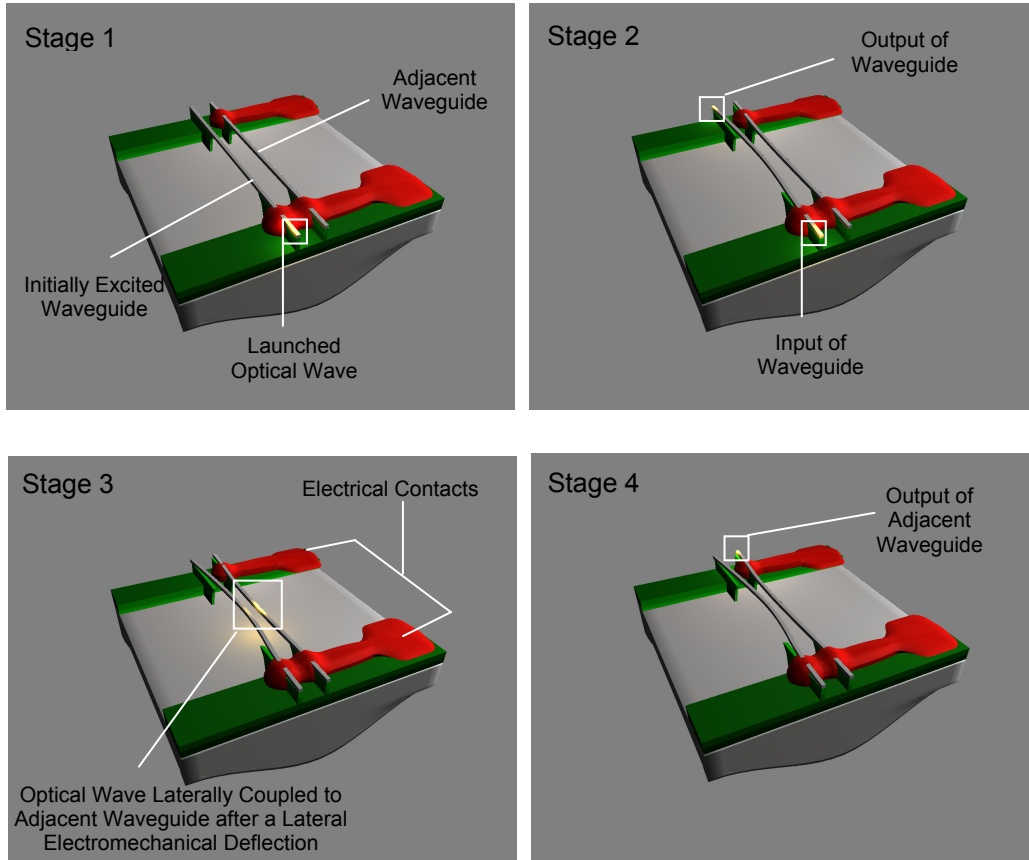
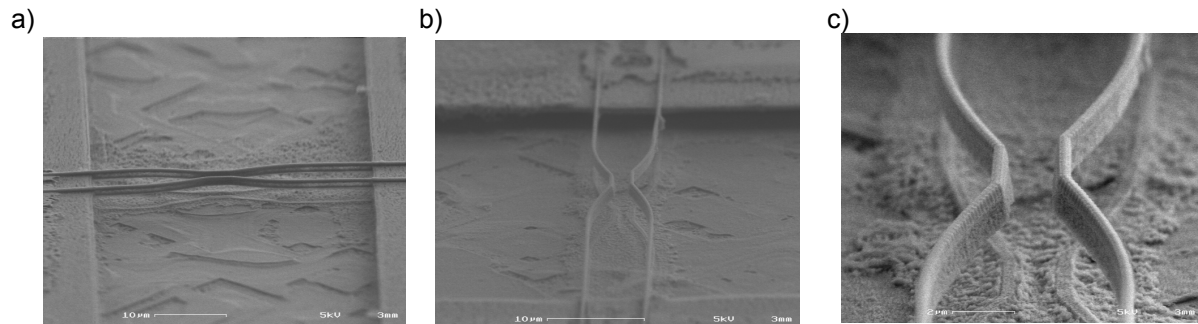


Figure 15. Three-dimensional rendering of the proposed ONEM device at four stages of operation.



Figures 16. SEM images of a fabricated ONEMS device in a gallium arsenide-based material system with an exponentially tapered geometry.

Publications

Journal Articles, Published

D.J. Ripin, J.T. Gopinath, H.M. Shen, A.A. Erchak, G.S. Petrich, L.A. Kolodziejski, F.X. Kaertner, and E.P. Ippen "Oxidized GaAs/AlAs mirror with a quantum-well saturable absorber for ultrashort-pulse Cr⁴⁺:YAG laser," *Optics Communications*, 214(1-6): 285-289, (2002).

Journal Articles, Submitted

P. Bienstman, S. Assefa, S.J. Johnson, J.D. Joannopoulos, G.S. Petrich, and L.A. Kolodziejski "Taper Structures for Coupling into Photonic Crystal Slab Waveguides," submitted to *Journal of Lightwave Technology*.

M. Povinelli, R. Bryant, S. Johnson, J. D. Joannopoulos, S. Fan, A. Erchak, E. Lidorikis, E. P. Ippen, G. S. Petrich "Design of a Nano-Electromechanical, High-Index-Contrast Guided-Wave Optical Switch for Single-Mode Operation at 1.55 μ m," submitted to *IEEE Photonics Technology Letters*.

Meeting Papers, Published

D.J. Ripin, J.T. Gopinath, H.M. Shen, F.X. Kaertner, E.P. Ippen A.A. Erchak, G.S. Petrich, and L. A. Kolodziejski, "A few-cycle Cr⁴⁺:YAG laser," Technical Digest. Summaries of papers presented at the Conference on Lasers and Electro-Optics 2002 Opt. Soc. America, Washington, DC,: 23 -23 (2002).

A.A. Erchak, D.J. Ripin, J.T. Gopinath, H.M. Shen, F.X. Kaertner, G.S. Petrich, L. A. Kolodziejski, and E.P. Ippen "Large Scale Oxidation of AlAs Layers for Broadband Saturable Bragg Reflectors," Technical Digest. Summaries of papers presented at the Conference on Lasers and Electro-Optics 2002 Opt. Soc. America, Washington, DC,: 225 (2002).

A. A. Erchak, S. Fan, P. Rakich, D. J. Ripin, G. S. Petrich, J. D. Joannopoulos, L. A. Kolodziejski, E. P. Ippen, "Emission from a two-dimensional photonic crystal: enhanced extraction of light and lasing action," Technical Digest. Summaries of papers presented at the Conference on Lasers and Electro-Optics 2002 Opt. Soc. America, Washington, DC,: 189-190, (2002)

References

- [1] D. Cotter, R.J. Manning, K.J. Blow, A.D. Ellis, A.E. Kelly, D.Nesset, I.D. Phillips, A.J. Poustie, D.C. Rogers, "Nonlinear Optics for High-Speed Digital Information Processing", *Science*, Vol. 286 (1999) 1523
- [2] D.J. Ripin, J.T. Gopinath, H.M. Shen, A.A. Erchak, G.S. Petrich, L.A. Kolodziejski, F.X. Kartner, E.P. Ippen, "Oxidized GaAs/AlAs mirror with a quantum-well saturable absorber for ultrashort-pulse Cr⁴⁺:YAG Laser," *Optics Communications*, 214(1-6), 285-289, 2002.
- [3] A.A. Erchak, D.J. Ripin, J.T. Gopinath, H.M. Shen, F.X. Kaertner, G.S. Petrich, L.A. Kolodziejski, and E.P. Ippen, "Large Scale Oxidation of AlAs Layers for Broadband Saturable Bragg Reflectors," *Lasers and Electro-Optics*, 2002. CLEO '02. Technical Digest. Summaries of Papers Presented at the, 225 (2002).
- [4] S.N. Tandon, J.T. Gopinath, T.R. Schibli, G.S. Petrich, L.A. Kolodziejski, F.X. Kaertner, and E.P. Ippen, "Saturable Absorbers with Large Area Broadband Bragg Reflectors for Femtosecond Pulse Generation," accepted to CLEO 2003.